# Self-assembled alkali and alkaline earth metal nanopatterns on $Fe_3O_4(001)$

G. Mariotto,* S. F. Ceballos, S. Murphy, N. Berdunov, C. Seoighe, and I. V. Shvets
*SFI Trinity Nanoscience Laboratory, Trinity College, Dublin 2, Ireland*
(Received 19 September 2003; published 29 July 2004)

We have studied the mechanism of nanopattern formation by self-assembly of impurities aggregated on the $Fe_3O_4(001)$ surface. Self-assembly was controlled by thermal diffusion from the bulk of natural and artificial single crystals. We show that the diffusion of potassium and calcium is of fundamental importance to the surface dynamics of magnetite. The self-assembly of Ca and K impurities, combined with the reduction in oxygen concentration, leads to the formation of nanotrenches that can be identified as a $p(1\times4)$ structure. According to our model, the formation of nanotrenches contributes in two ways to the reduction of the surface energy. Firstly, alkali and alkaline earth impurities cause a reduction of the strain energy due to their large ionic radii. Secondly, their segregation and the reduction of the O/Fe ratio at the surface cause a reduction of the surface polarity. The structure of ordered nanotrenches could be used as a template for the deposition of carbon nanotubes, fullerenes, and DNA molecules.

DOI: 10.1103/PhysRevB.70.035417 PACS number(s): 68.35.Fx, 66.30.Jt, 68.37.Ef

## I. INTRODUCTION

Nanostructures, with dimensions in the nanometer and atomic range, may become the building blocks of future electronic, mechanical, and optical devices. The conventional methods of microfabrication, e.g., lithographic methods, are limited in their resolution and new techniques to manipulate atoms and molecules to ultimately fabricate nanodevices are being developed.[1] Molecular manipulation using scanning probe microscopy has been demonstrated, but this method is far too slow and awkward to have industrial applications. Self-assembly of atoms and molecules into nanostructures is an attractive means of nanofabrication. Self-assembly is typically based on the deposition of an adlayer on a properly chosen substrate under well-defined conditions, using, e.g., molecular-beam epitaxy (MBE). An alternative method is that of controlled diffusion of impurities from the bulk of a single crystal to the surface or, in the case of thin films, from the substrate into the film. This method has not been investigated thoroughly so far. The purpose of the present study is to explore the physical mechanisms of self-assembly by controlled diffusion of impurities from the bulk to the $Fe_3O_4(001)$ surface. Magnetite is a particularly well suited material for these studies. The $Fe_3O_4(001)$ surface is a polar surface[2] and is susceptible to significant transformations driven by charge compensation to minimize the surface energy. In this work, we will show that segregation of K and Ca at the surface by thermal diffusion takes place in single crystals from different sources grown by different techniques. K and Ca are present in the bulk only in small concentrations. However, they play a crucial role in the formation of the surface of a magnetite crystal. This is due to the fact that K and Ca cannot be accommodated in a spinel structure, as these ions are too large to fit into the interstitial sites between the oxygen anions. Therefore, they diffuse to the surface during the anneal, causing the formation of self-assembled structures.

Induced surface reconstructions of alkali and alkaline earth metals have been observed on a range of different systems, such as thin films of $Fe_3O_4$ grown on MgO(001) substrates,[3,4] thin films of $Fe_3O_4$ grown on Pt(111) substrates,[5] and $TiO_2$ single crystals.[6,7] A $p(1\times4)$ reconstruction was observed by Anderson *et al.*[3] on a 1-$\mu$m-thick film of magnetite grown on a MgO(001) substrate. A similar effect was observed by Voogt,[8] who reported a $p(1\times3)$ reconstruction on magnetite films grown on MgO(001). Anderson *et al.* attributed the surface reconstruction to the segregation of magnesium from the substrate, leading to the formation of a $MgFe_2O_4$ phase. Gao *et al.*[9] in a study of magnetite thin films grown on MgO(001), suggested that the Mg ions diffuse through the crystal lattice via vacancies in the octahedral cation sublattice. Once they reach the surface, they decorate the rows of octahedral *B*-site cations. Nörenberg *et al.*[7] have investigated the Ca-induced surface reconstruction on $TiO_2$, observing both $p(1\times3)$ and $p(1\times4)$ phases. They attributed the $p(1\times3)$ reconstruction to $Ca^{2+}$ cations replacing the Ti cations at the surface of the crystal. The $p(1\times3)$ phase was replaced by a $p(1\times4)$ missing row structure due to oxygen loss from the surface.

Magnetite ($Fe_3O_4$) is an inverse spinel material, with the formula $[Fe^{3+}]_A[Fe^{2+}Fe^{3+}]_BO_4^{2-}$, where *A* and *B*, respectively, denote the tetrahedral and octahedral coordinations of the cation sites within the fcc lattice formed by the larger oxygen anions. The lattice constant of magnetite is $a=8.3963$ Å,[10] with a repeat unit cell that contains 32 $O^{2-}$ anions, eight $Fe^{3+}$ cations in tetrahedral *A* sites, and eight $Fe^{2+}$ and eight $Fe^{3+}$ cations in the octahedral *B* sites (see Fig. 1). The separation between adjacent *A*–*A* or *B*–*B* planes is ~2.1 Å, while the separation between adjacent *A* and *B* planes is ~1.05 Å. The nearest-neighbor cations at *B* sites form rows running along the $\langle110\rangle$ directions. *B* planes separated by 2.1 Å or an odd multiple of this value contain rows that are oriented by 90° with respect to each other. At room temperature, magnetite is a moderately good conductor, with a conductivity of $\sigma \approx 200\ \Omega^{-1}\,\mathrm{cm}^{-1}$. At around 125 K, stoichiometric magnetite undergoes a first-order phase transition, known as the Verwey transition, and its conductivity decreases by about two orders of magnitude. Magnetite is a highly interesting mate-

 

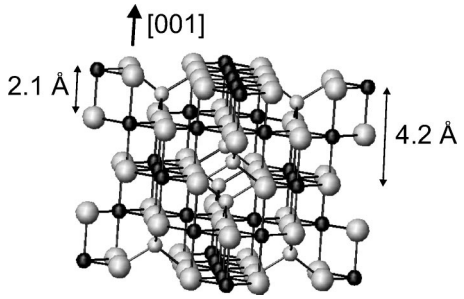


FIG. 1. Ball and stick model of the conventional unit cell of magnetite. The large gray spheres represent the oxygen anions, the small gray spheres represent the $Fe^{3+}$ cations in tetrahedral coordination (*A* sites) and the small black spheres stand for $Fe^{2+}$ and $Fe^{3+}$ cations in octahedral coordination (*B* sites).

rial for applications in spin electronics, thanks to its half-metallic properties.[11] Recently, there has been a rapidly growing interest in heterojunctions using magnetite layers for emerging spin electronics technologies. However, the complexity of the surface is a serious impediment, as the surface morphology on the nanometer and atomic scale affects its electronic and magnetic properties. The matter is complicated by the rather large unit cell of $Fe_3O_4$ and the fact that the spinel structure of magnetite lends itself to a large number of subtle variations. For example, FeO, $Fe_3O_4$, and $\gamma$-$Fe_2O_3$ can readily transform into each other under suitable anneal conditions. Although $Fe_3O_4$ and $\gamma$-$Fe_2O_3$ have a similar crystallographic structure and are difficult to distinguish using x-ray diffraction (XRD), their electronic properties are completely different. Transformations between different iron oxides have been studied extensively in the bulk, but studies of such transformations at surfaces and interfaces are yet at an early stage. This study is a contribution into the mechanism of self-assembly as well as into the complex area of the structure of the magnetite surface on the nanometer and atomic scale.

## II. EXPERIMENTAL

### A. *Ex situ* characterization and preparation

A set of artificial and natural single crystals has been used in these experiments. The artificial crystals were grown employing the skull melting technique.[12] The natural crystals originated from Zillertal, Austria. The crystals were aligned with a precision of ±1° with respect to the (001) crystallographic plane and oriented along the [010] direction. The artificial crystals were characterized by powder XRD and resistance versus temperature measurements. The diffractograms showed good agreement with the reference spectra for magnetite, and a lattice constant of $8.40 \pm 0.01$ Å was measured. A four-point resistance versus temperature measurement was performed on an artificial crystal, giving a Verwey transition temperature of 108 K, indicating that the crystal was substoichiometric.[13] The electrical conductivity at room temperature was found to be $\sigma \approx 116\ \Omega^{-1}\,\mathrm{cm}^{-1}$, comparable with the literature data. The natural crystals were part of the single crystalline nugget used by Tarrach *et al.*[14] A lattice constant of $8.41 \pm 0.01$ Å and a Verwey transition temperature of 98 K were measured for these crystals. Raman spectra of these crystals were consistent with magnetite reference spectra and indicated that the crystals did not contain other phases of iron oxides. Magnetization measurements using vibrating sample magnetometer resulted in the value of $M_S = 100.9$ emu/g, which again indicates that the crystals were of $Fe_3O_4$ phase.

The crystals were mechanically polished using diamond paste with a grain size down to 0.25 $\mu$m. After rinsing them in ethanol, the crystals were secured onto a Mo sample holder and inserted into the UHV system.

### B. *In situ* characterization and preparation

The experiments were performed in a UHV system with a base pressure of $\sim 5 \times 10^{-11}$ mbar, equipped with a scanning tunneling microscope (STM), low-energy electron diffraction (LEED), and Auger electron spectroscopy (AES) setups. The preparation chamber was equipped with a resistive heater for annealing samples up to 1100 K, a cold-cathode ion gun for $Ar^+$ ion etching crystals and precision leak valves for the introduction of high purity oxygen, argon, and hydrogen gases. The crystals were annealed to a temperature of $990 \pm 10$ K, as measured by a *K*-type thermocouple attached to the heating stage.

AES measurements were carried out using a cylindrical mirror analyzer from Physical Electronics. Spectra between 0 and 750 eV were collected using a 3 keV beam energy. The typical target current values ranged between 2 and 4 $\mu$A. The spectra were acquired in derivative mode using lock-in detection and a 12 kHz sinusoidal reference signal. All concentrations measured by AES are expressed in atomic percent.

LEED analysis was performed using a RVLO 900 four-grid reverse-view optics (VG Microtech), operated at primary beam energies between 40 and 100 eV, with a typical emission current of 0.5 mA.

STM measurements were performed in constant-current mode. A bias voltage ranging from +0.6 to +1 V was applied to the sample, and the tunneling current was varied between 0.1 and 0.3 nA. A bias voltage of +1 V and a tunneling current of +0.1 nA were found to provide the most stable tunneling conditions. Scanning with a negative bias was attempted, but did not result in a stable tunneling current. Four different types of tips were used during these experiments: PtIr, W, Fe, and MnNi. PtIr tips were prepared by mechanical cutting and did not require any further treatment. W, Fe, and MnNi tips were electrochemically etched and then ion-etched in vacuum with 1-kV $Ar^+$ ions to remove oxide layers prior to use. The procedure for the fabrication of MnNi tips was developed in our laboratory.[15,16]

## III. RESULTS AND DISCUSSION

### A. $(\sqrt{2} \times \sqrt{2})R45°$ reconstruction

A $(\sqrt{2} \times \sqrt{2})R45°$ reconstruction has been observed by several groups on both natural and artificial single crystals,[17,18] and on thin films grown by MBE.[9,19,20] Different

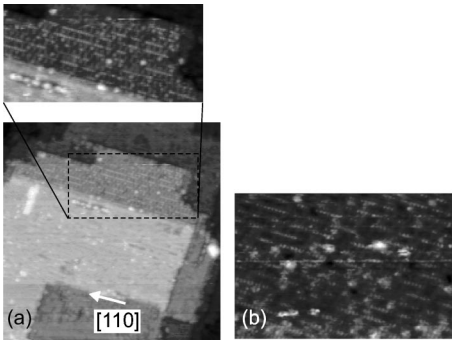


FIG. 2. (a) $(600\times600)$ Å$^2$ STM image of an artificial $Fe_3O_4(001)$ single crystal. A $(340\times190)$ Å$^2$ zoom is shown. (b) $(300\times200)$ Å$^2$ STM image. The atomic rows are shown in more detail. The periodicity along the [110] direction is ~6 Å, and adjacent rows are separated by ~18 Å.

models have been proposed to explain this reconstruction,[18–21] based on either Tasker's electrostatic model[2] or on the electron counting model.[22] We have recently described a preparation procedure, consisting of $Ar^+$ ion sputtering and a combination of annealing in oxygen atmosphere and UHV, which gives rise to a contaminant free surface. We have established that the $Fe_3O_4(001)$ surface terminates at the *B* plane, exposing rows of Fe ions running along the [110] direction, and we have proposed an explanation of the reconstruction observed in terms of charge ordering at the *B* sites.[23] We have also established that the $(\sqrt{2}\times\sqrt{2})R45°$ reconstruction is disrupted as contamination of the surface occurs.

### B. p(1×3) reconstruction

A $p(1\times3)$ reconstruction has been occasionally observed after annealing the crystal in UHV at a temperature of $990\pm10$ K. STM images of an atomically resolved $p(1\times3)$ reconstruction are shown in Figs. 2(a) and 2(b). Atomic rows are visible along the [110] direction; the periodicity along these rows is ~6 Å, and adjacent rows are separated by ~18 Å. The rows are rotated by 90° on terraces separated by an odd multiple of 2.1 Å, which clearly indicates a *B*-plane-terminated surface. The 90° rotation of these domains gives rise to the LEED pattern shown in Fig. 3(a), where the $p(1\times3)$ superlattice is clearly visible. We have attributed the $p(1\times3)$ reconstruction to the segregation of Ca and K ions, replacing Fe ions in octahedral coordination. A schematic of the reconstruction is shown in Fig. 4.

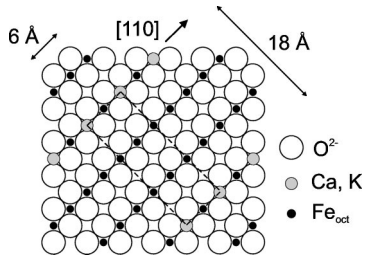


FIG. 4. A schematic showing the $p(1\times3)$ reconstruction due to Ca and K ions replacing Fe ions in octahedral coordination. The $p(1\times3)$ superlattice is marked by a dashed rectangle.

AES data show the presence of K and Ca contaminants on the surface of the crystal [see Fig. 3(b)]. A Ca peak at 292 eV and a K peak at 249 eV are visible, corresponding to ~5.7% and ~1.5% concentrations, respectively. A similar concentration of Ca and K was detected on a surface exhibiting a $p(1\times4)$ reconstruction (see Sec. III C). However, contrary to the $p(1\times4)$ reconstruction, no reduction of the surface was detected, and the O/Fe ratio was measured to be 1.3, in accordance with the value of a stoichiometric surface. Oxygen vacancies do not therefore play a role in the formation of the $p(1\times3)$ reconstruction, which is solely induced by the segregation of contaminants to the surface.

### C. p(1×4) reconstruction

A $p(1\times4)$ reconstruction has been found to set after long annealing sessions. This was found to be a very stable condition, and once established, it persisted so that mechanical polishing of the crystal was required to remove this reconstruction.

Figure 5(a) shows a typical image of a clean $Fe_3O_4(001)$ surface, prepared by annealing for 5 h in UHV at $990\pm10$ K. The surface is characterized by flat terraces with edges aligned along the [110] and $[\bar{1}10]$ directions and separated by integer multiples of 2.1 Å along the [001] crystallographic axes. Further annealing in UHV causes trenches to appear on the surface. Some of these trenches are indicated by the black arrows in Fig. 5(b). Further transformation of

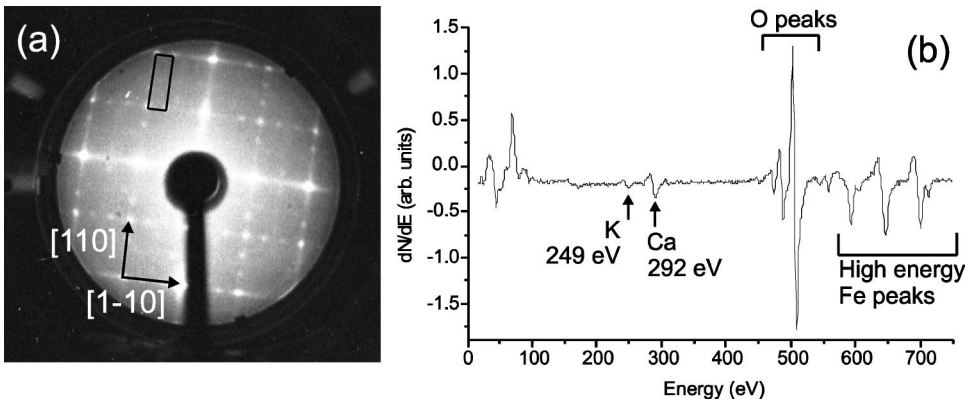


FIG. 3. (a) LEED pattern observed with a primary electron energy of 47 eV. The $p(1\times3)$ reconstruction is clearly visible and is highlighted by a black rectangle. (b) AES spectrum. The potassium and calcium peaks are visible at 249 and 292 eV, respectively.

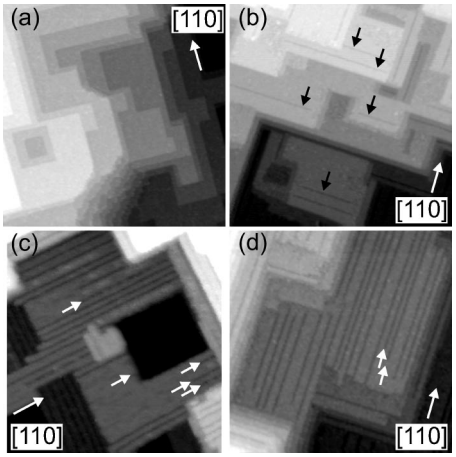


FIG. 5. Dynamics of the transformation of the $Fe_3O_4(001)$ surface from flat terraces to an ordered array of nanotrenches. (a) $(2000\times2000)$ Å$^2$ STM image. The surface is characterized by flat terraces. (b) $(1000\times1000)$ Å$^2$ STM image. Some of the trenches start to appear, as shown by the black arrows. (c) $(1000\times1000)$ Å$^2$ STM image. The trenches on the surface start at one step edge to propagate along the [110] or $[1\bar{1}0]$ direction. While most of the trenches run through the full length of the terrace, some terminate in the middle of the terraces, as indicated by the white arrows. (d) $(1000\times1000)$ Å$^2$ STM image. A 90° rotation of the trenches is observed on subsequent terraces separated by a 2.1 Å height difference. This is consistent with the octahedrally terminated surface of magnetite.

the surface corresponding to progressively longer annealing times is shown in Figs. 5(c) and 5(d). In Fig. 5(c), the number of trenches on the terraces has increased. The separation between the trenches is not regular, but varies among 22, 35, and 50 Å. The trenches start at step-edges and propagate along the [110] or $[1\bar{1}0]$ direction. While most of the trenches run through the full length of the terrace, some terminate in the middle of the terrace, as indicated by the white arrows in Fig. 5(c). A 90° rotation of the trenches is observed on subsequent terraces separated by 2.1 Å height difference. This is expected for a surface exhibiting a twofold symmetry, such as the octahedrally terminated surface of $Fe_3O_4(001)$. Since a 90° rotation of the trenches has never been observed on the same terrace, we conclude that the surface is terminated at the *B* plane, and that the rows of octahedral irons dictate the propagation of the trenches along the [110] and $[1\bar{1}0]$ directions.

We have collected extensive experimental data to establish the nature of the reconstruction observed.[24] Successive annealing cycles have been carried out to investigate the dynamics of the formation of the trenches on the surface. STM, LEED, and AES results provide strong evidence that the $p(1\times4)$ reconstruction is a result of a major surface rearrangement at the nanometer scale.

Two concomitant factors, a reduction in the O/Fe ratio and the diffusion of Ca and K contaminants to the surface of the crystal, play a crucial role in the formation of the $p(1\times4)$ reconstruction. Both effects are caused by thermal annealing and lead to a greater density of trenches on the surface. This effect is illustrated in the histogram shown in Fig.

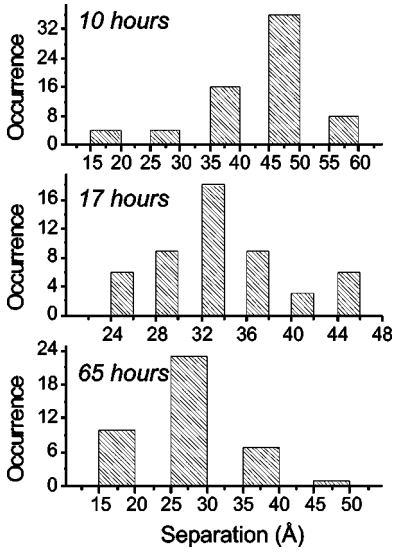


FIG. 6. Series of histograms showing the separation between trenches on the surface after 10, 17, and 65 h annealing times at 1000 K. The separation decreases as the anneal time increases.

6. Eventually the flat terraces transform completely into an array of trenches. An example of this surface is shown in Figs. 7(a) and 7(b). The periodicity of the rows ranges between 24 and 26 Å. The corrugation across the rows is $1.4\pm0.1$ Å. This structure was observed on both natural and artificial crystals prepared in the same manner. Figure 7(c) shows a $(2000\times2000)$ Å$^2$ STM image displayed in derivative mode. The periodicity of the rows is highly regular [Fig. 7(d)]. It was found that the onset of the surface reconstruction is locally dependent and that different areas of the crystal reconstruct at different rates, indicating an uneven distri-

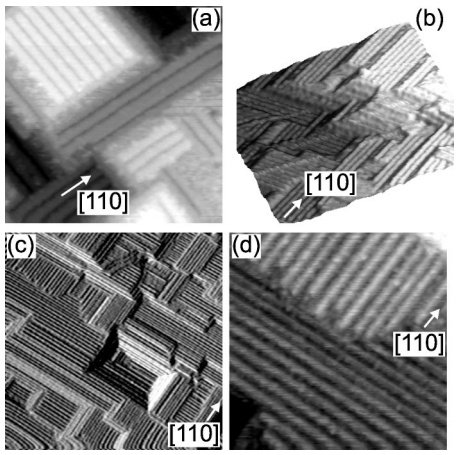


FIG. 7. (a) $(500\times500)$ Å$^2$ STM image. (b) $(1000\times1000)$ Å$^2$ STM image. Terraces separated by an odd multiple of 2.1 Å exhibit a 90° rotation of the rows that are oriented along the [110] or $[1\bar{1}0]$ direction. The periodicity of the rows ranges between 24 and 26 Å. A MnNi tip was used to scan the surface. (c) $(2000\times2000)$ Å$^2$ STM image of a natural crystal of magnetite displayed in derivative mode. (d) $(500\times500)$ Å$^2$ STM image of a natural crystal of magnetite. The step height between the two terraces is $2.1\pm0.2$ Å along the *z* direction. An Fe tip was used to scan the surface.

TABLE I. The annealing conditions during four annealing cycles, together with the relative concentrations of the contaminants detected on the surface.

| Anneal cycle | Anneal temp. (K) | K level (%) | Ca level (%) |
|---|---|---|---|
| I | 990±10 | 1.9 | 5.4 |
| II | 990±10 | 0.9 | 6.7 |
| III | 990±10 | 0.6 | 7.8 |
| IV | 1030±10 | ··· | 9.5 |

bution of impurities across the sample surface.

The links among the annealing of the crystals, the segregation of contaminants to the surface, and the decrease of the O/Fe ratio are supported by AES data. An artificial $Fe_3O_4$ crystal was annealed in UHV at a temperature of 990±10 K. Four consecutive annealing cycles were analyzed. Atomic concentrations corresponding to the four cycles are shown in Table I.

After the first annealing cycle, the AES spectrum shown in Fig. 8(a) was acquired. The only impurities detected on the surface were a 1.9% concentration of potassium, detected at 249 eV, and a 5.4% concentration of calcium at 292 eV. Figure 9(a) shows the LEED pattern recorded from this surface. The $p(1\times1)$ unit cell is indicated by the solid square labeled "A." The lattice constant was measured to be 6.0±1.2 Å, in agreement with the expected value for the primitive unit cell of magnetite (i.e., the spacing along the [110] direction). The LEED pattern indicates the coexistence of domains of two reconstructions on the surface. Satellite spots are clearly visible along the [110] and $[1\bar{1}0]$ directions around the primary spots. Their separation is ~1/4 of that between the integral order spots, and corresponds to a $p(1\times4)$ reconstruction with domains oriented by 90° with respect to each other. The $p(1\times4)$ superlattice is marked by the solid rectangle labeled "B" in Fig. 9(a), and a schematic is shown in Fig. 9(b). In addition to the $p(1\times4)$ reconstruction, the presence of a $(\sqrt{2}\times\sqrt{2})R45°$ reconstruction is indicated by faint fractional spots marked by the white arrows in Fig. 9(a). We attribute this reconstruction—usually observed on a clean $Fe_3O_4(001)$ surface[18,23,25]—to the crystal planes lying beneath the topmost layers contaminated with calcium

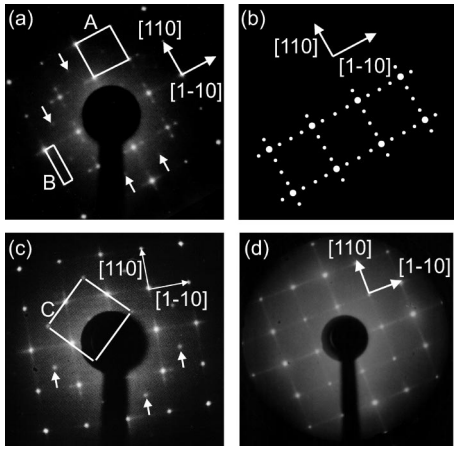


FIG. 9. First annealing cycle: LEED pattern observed with a primary electron energy of 93 eV. Satellite spots are visible around the primary spots along the [110] and $[1\bar{1}0]$ directions. Faint spots corresponding to a $(\sqrt{2}\times\sqrt{2})R45°$ reconstruction are indicated by white arrows. (b) Schematic of the $p(1\times4)$ reconstruction. (c) Second annealing cycle: LEED pattern observed with a primary electron energy of 93 eV. Satellite spots are still visible around the primary spots, but some of them form streaked lines along the [110] and $[1\bar{1}0]$ directions. The $(\sqrt{2}\times\sqrt{2})R45°$ mesh is now clearly visible. (d) Fourth annealing cycle: LEED pattern observed with a primary electron energy of 66 eV. No superlattice is visible on the surface.

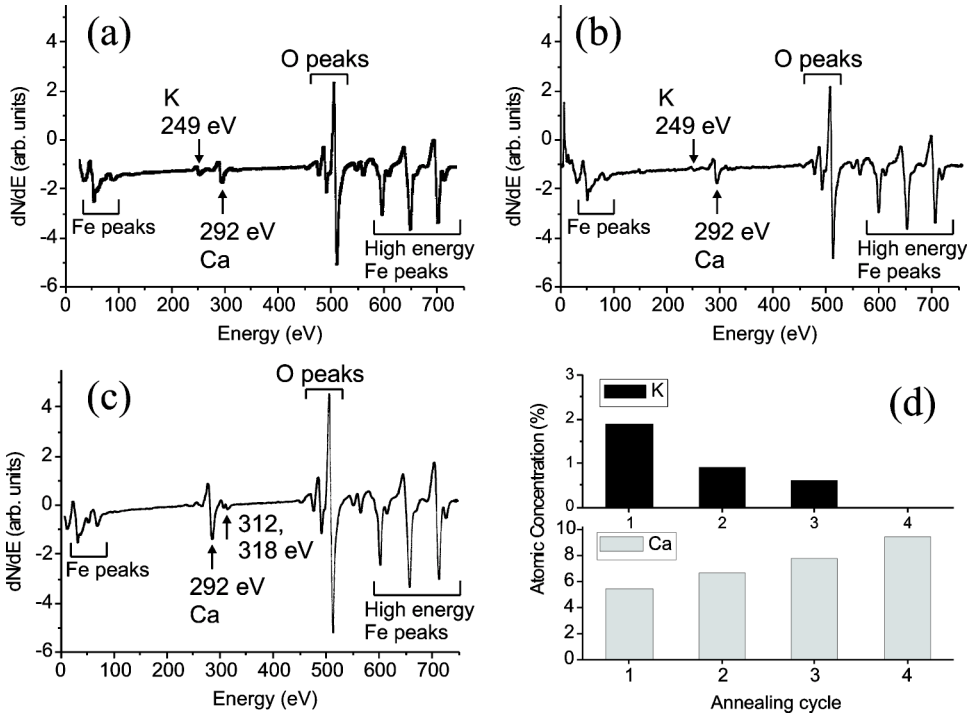


FIG. 8. Auger spectra corresponding to the first (a), second (b), and fourth annealing cycle (c). The potassium and calcium peaks are visible at 249 and 292 eV, respectively. (d) indicates the change in the K and Ca concentrations after the four annealing cycles.

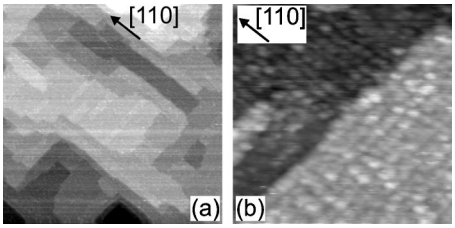


FIG. 10. (a) $(2000\times2000)$ Å$^2$ STM image of an artificial $Fe_3O_4(001)$ single crystal after the first annealing cycle. (b) $(400\times400)$ Å$^2$ STM image. Two terraces separated by $2.1\pm0.2$ Å along the *z* direction are visible; the rows on the two terraces are rotated by 90° with respect to each other. All images were acquired at a sample bias of 1.0 V and a tunneling current of 0.1 nA using a W tip.

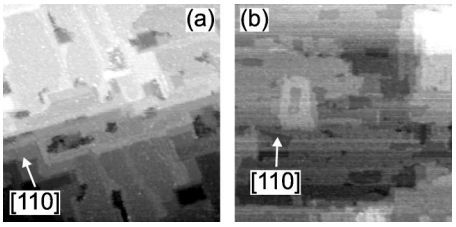


FIG. 12. (a) Surface after the third annealing cycle: $(2000\times2000)$ Å$^2$ STM image. Terrace edges have become rough and the rows are no longer visible. (b) Surface after the fourth annealing cycle: $(2000\times2000)$ Å$^2$ STM image. The terrace definition is almost completely lost. A $p(1\times1)$ LEED pattern [see Fig. 9(d)] was observed.

and potassium. The surface is characterized by the presence of mostly well-defined terraces covered by rows running along the [110] and [1$\bar{1}$0] directions, as shown in Figs. 10(a) and 10(b). The orientation of the rows changes by 90° on each two subsequent terraces separated by a 2.1 Å height difference. The separation between the rows varies between 22 and 30 Å, and the corrugation in the direction perpendicular to the rows ranges between 1 and 2 Å.

Figure 8(b) shows the Auger spectrum taken after the crystal was further annealed in UHV at $990\pm10$ K. A comparison of the atomic concentrations with the first annealing cycle shows an increase of the Ca concentration and a decrease in the K concentration [see Fig. 8(d)]. The corresponding LEED pattern is shown in Fig. 9(c). The pattern is similar to the one obtained after the first annealing cycle, with streaked fractional-order spots along the [110] and [1$\bar{1}$0] directions. Figure 11(a) shows a $(700\times750)$ Å$^2$ STM image of this surface. Two different types of terraces can be identified, both having the edges aligned along the [110] and [1$\bar{1}$0] directions. Terraces labeled as "$B_0$," "$B_1$," and "$B_2$" correspond to octahedral planes and are characterized by alternating bright and dark rows oriented along the [110] direction, while terraces labeled as "$A_0$" and "$A_1$" correspond to tetrahedral planes and are flat. This observation is in agreement with the fact that trenches are expected to form on octahedral terraces only, since tetrahedral planes do not contain oxygen atoms. The step height between terraces labeled as "*B*" and terraces labeled as "*A*" is ~1 Å, which is the value expected for the distance between two adjacent octahedral and tetrahedral atomic planes in bulk magnetite [see the line profile in Fig. 11(b)]. The rows on terraces $B_1$ and $B_2$ are regularly spaced and their average periodicity was measured to be $26\pm3.0$ Å, while the corrugation perpendicular to the rows varies between 1 and 2 Å.

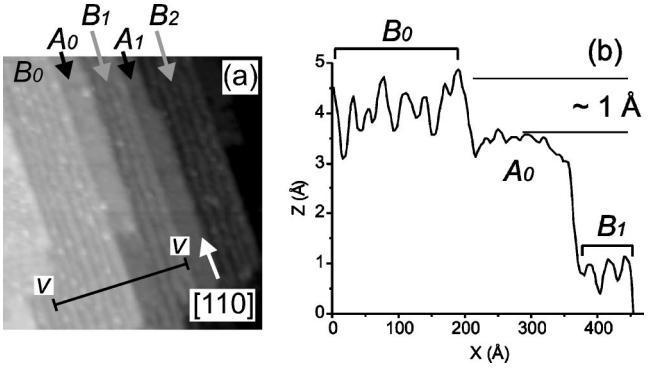


FIG. 11. (a) $(700\times750)$ Å$^2$ STM image taken after the second annealing cycle. Terraces labeled as "*B*" correspond to octahedral planes and are characterized by rows running along the [110] direction, while terraces labeled as "*A*" correspond to tetrahedral planes and are flat. The step height between terraces *B* and *A* is ~1 Å. The step height between *B* terraces is $4.2\pm0.4$ Å. (b) Line profile showing a ~1 Å step height between terraces *B* and *A*.

The crystal was further annealed in UHV at $990\pm10$ K. The Auger spectrum shows a further increase of the calcium concentration up to 7.8%; trace amounts of potassium are still detected and a small sulphur peak appears (see Table I). A $(2000\times2000)$ Å$^2$ STM image is shown in Fig. 12(a). The terrace edges have become rough and rows are no longer visible on the terraces. The step height between adjacent terraces is a multiple of ~2 Å. Further annealing in UHV produced a surface where the terrace definition is almost completely lost, as shown in Fig. 12(b). The concentration of calcium increased further, reaching a value of 9.5 at.%. No traces of potassium or sulphur were detected [Fig. 8(c)]. A $p(1\times1)$ LEED pattern was observed [see Fig. 9(d)]. The streaked lines around the primary spots along the [110] and [1$\bar{1}$0] directions are no longer visible, and the additional diffraction spots of the $(\sqrt{2}\times\sqrt{2})R45°$ reconstruction are also lost.

Our data show that long annealing cycles in UHV caused the onset of a reconstruction characterized by the appearance of trenches aligned along the [110] direction. The separation between the trenches is highly irregular at first, giving rise to what can be called a $p(1\times n)$ reconstruction. As the annealing time increases, the separation between the trenches becomes more regular, eventually giving rise to an almost regular $p(1\times4)$ reconstruction. Our data show that the driving forces causing such a reconstruction are to be identified with an increase in the contaminants' concentration at the surface and a decrease of the O/Fe ratio. The segregation mechanism for metallic systems can be explained in terms of the size accommodation model.[26] In this model, segregation is driven by the decrease in elastic strain energy as solute atoms—either too big or too small—diffuse from the bulk and occupy an interface site with less strain. Table II shows

TABLE II. Ionic radii of K, Ca, and Fe in tetrahedral and octahedral coordination. The Fe ions are assumed to be in the high-spin state.

| $K^{+}_{tetr}$ (pm) | $K^{+}_{oct}$ (pm) | $Ca^{2+}_{oct}$ (pm) | $Fe^{2+}_{oct}$ (pm) | $Fe^{3+}_{oct}$ (pm) | $Fe^{3+}_{tetr}$ (pm) |
|---|---|---|---|---|---|
| 151 | 152 | 114 | 92 | 78.5 | 63 |

that the ionic radii of Ca and K ions are much larger than those of Fe ions.[27] It is therefore expected that Ca and K ions will segregate at the surface of the $Fe_3O_4$ crystals.

The decrease of the O/Fe ratio suggests that, due to the long annealing in UHV, the surface of the crystal is reduced and oxygen vacancies are created at the surface. This interpretation is backed up by our experimental data. The O/Fe ratios corresponding to the AES spectra of Figs. 8(a)–8(c), were measured to be 1.1, 0.9, and 0.8, respectively. The typical O/Fe ratio measured for a clean surface, exhibiting a $(\sqrt{2}\times\sqrt{2})R45°$ reconstruction, is 1.3. By taking this into account, it is clear that a significant reduction of the surface is induced by long anneals. The decrease of the O/Fe ratio correlates well with the increasing anneal time and the consequent increase in the density of trenches on the surface.

To give rise to the structure observed by STM, the oxygen vacancies are arranged around the Ca and K ions, which relax back into the surface due to the broken bonds with the oxygen ions. A schematic of the $p(1\times4)$ reconstruction is shown in Fig. 13. The removal of oxygen ions bound to $Ca^{2+}_{oct}$ and $K^{+}_{oct}$ ions accounts for the anisotropic direction of the trenches observed on the terraces. The model proposed by us is in agreement with the AES, STM, and LEED data we have collected. STM data provide evidence of a surface terminated at the octahedral plane and show a very good correlation between the appearance of trenches and the reduction in the O/Fe ratio at the surface. Furthermore, in the cases in which a tetrahedral termination was observed, no trenches running along the [110] direction were observed on the *A* planes. Since the tetrahedral planes do not contain oxygen atoms, this fact corroborates our explanation that one of the principal factors causing trenches to appear are oxygen vacancies. LEED data show that the oxygen vacancies are distributed in an ordered fashion that gives rise to the structure observed by STM and in agreement with the model shown in Fig. 13.

To summarize, the dynamics of trench formation is due to the segregation of K and Ca to the surface and to a reduction of the O/Fe ratio at the surface. Continued annealing produces a Ca and K buildup on the surface to a point where the surface becomes saturated. To accommodate more impurities, the surface undergoes a gradual transformation, resulting in the formation of trenches. This type of termination provides a greater number of surface sites with respect to the flat surface. This mechanism is analogous to that behind the oxygen-induced missing row structure observed in the initial stages of oxidation of the W(001) surface.[28,29] The (001) bulk terminated surface of magnetite is *polar* and therefore is intrinsically unstable. In particular, the $Fe_3O_4(001)$ surface terminated at the octahedral plane has a shortage of charge due to the oxygen dangling bonds that are left empty. The formation of nanotrenches contributes to the reduction of the surface energy in two distinct ways. Firstly, oxygen vacancies created at the surface significantly lower the surface polarity. Secondly, alkali and alkaline earth impurities cause a reduction of the strain energy due to their large ionic radius, leading to an equidistant separation between the nanotrenches.

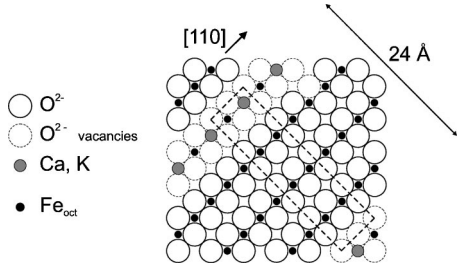


FIG. 13. A schematic of the $p(1\times4)$ reconstruction. Oxygen vacancies are created at the surface by the extended anneal.

## IV. CONCLUSIONS

The aim of this study was to investigate the segregation of alkali and alkaline earth metal impurities and their influence on the morphology of the $Fe_3O_4(001)$ surface. Segregation was induced by thermal annealing in UHV of artificial and natural single crystals of magnetite. We have found that the surface reconstructions of the $Fe_3O_4(001)$ surface are governed on one hand by the concentration of alkali and alkaline earth metals, and on the other hand by the decrease in the O/Fe ratio. The main results can be summarized as follows:

(1) A $p(1\times3)$ reconstruction was observed after annealing in UHV. AES data show the presence of both K and Ca on the surface of the crystal, as well as an O/Fe ratio of 1.3, indicating that no reduction of the surface had taken place. Due to their large ionic radii, Ca and K ions segregate at the surface to occupy interface sites with less strain. STM images provide evidence of a surface terminated at the octahedral plane, with rows of atoms forming nanowires along the [110] and $[1\bar{1}0]$ directions. We have proposed a schematic model to explain the $p(1\times3)$ reconstruction, in which Ca and K ions occupy octahedrally coordinated sites.

(2) After longer annealing sessions the $p(1\times3)$ reconstruction was replaced by the $p(1\times4)$ reconstruction, and the surface was characterized by trenches oriented along the [110] and $[1\bar{1}0]$ directions. AES showed a significant decrease in the O/Fe ratio as function of the annealing time. The density of trenches was found to be directly proportional to the decreasing oxygen concentration at the surface, indicating that the O/Fe ratio plays a crucial role in the formation of such a reconstruction.

(3) A concentration of Ca and K similar to the $p(1\times3)$ reconstruction was measured. However, it must be noted that the $p(1\times4)$ reconstruction is driven by a decrease in the O/Fe ratio and also by the segregation of contaminants at the surface, while in the $p(1\times3)$ reconstruction, only the latter factor plays a role.

(4) We therefore conclude that the surface reconstructions of $Fe_3O_4(001)$ are governed by two concomitant factors, the segregation of alkali and alkaline earth metals on one hand, and the decrease of the O/Fe ratio on the other hand. As a consequence, two different reconstructions may correspond to similar concentrations of Ca and K, provided the O/Fe ratio is different.

Nanoscale materials exhibit interesting physical and chemical properties. Since iron oxides are widely used as recording materials and photocatalysts, nanostructured oxides are of great interest. Our experiments show that the morphology of the (001) surface of magnetite can be controlled by the diffusion of alkali and alkaline earth metals. As the concentration of impurities contained in single crystals is hard to control, the use of thin films grown on suitable substrates may be a better choice for the formation of tailored nanotemplates. One could envisage the use of these highly ordered structures as nanotemplates for the deposition of carbon nanotubes, fullerenes, and DNA molecules, whose sizes are compatible with the typical dimensions of our nanotemplates.

## ACKNOWLEDGMENT

Financial assistance from Science Foundation Ireland (SFI), Contract No. 00/PI.1/C042 is gratefully acknowledged.

*Electronic address: mariotl@tcd.ie

[1] J. A. Stroscio and D. M. Eigler, Science **254**, 1319 (1991).
[2] P. W. Tasker, J. Phys. C **12**, 4977 (1979).
[3] J. Anderson, M. Kuhn, U. Diebold, K. Shaw, P. Stoyanov, and D. Lind, Phys. Rev. B **56**, 9902 (1997).
[4] K. Shaw, E. Lochner, and D. Lind, J. Appl. Phys. **87**, 1727 (2000).
[5] S. K. Shaikhutdinov, W. Weiss, and R. Schlögl, Appl. Surf. Sci. **161**, 497 (2000).
[6] L. Zhang, M. Li, and U. Diebold, Surf. Sci. **412/413**, 242 (1998).
[7] H. Nörenberg and J. H. Harding, Surf. Sci. **473**, 151 (2001).
[8] F. Voogt, Ph.D. thesis, University of Groningen, 1998.
[9] Y. Gao and S. A. Chambers, J. Cryst. Growth **174**, 446 (1997).
[10] R. W. G. Wyckoff, *Crystal Structures*, 2nd ed. (Interscience, New York, 1964).
[11] A. Gupta and J. Z. Sun, J. Magn. Magn. Mater. **200**, 24 (1999).
[12] J. M. Honig, J. Alloys Compd. **229**, 24 (1995).
[13] R. Aragon, R. J. Rasmussen, J. P. Shepherd, J. W. Koenitzer, and J. M. Honig, J. Magn. Magn. Mater. **54-57**, 1335 (1986).
[14] R. Wiesendanger, I. V. Shvets, D. Bürgler, G. Tarrach, H. J. Güntherodt, J. M. D. Coey, and S. Gräser, Science **255**, 583 (1992).
[15] S. Murphy, J. Osing, and I. V. Shvets, J. Magn. Magn. Mater. **198-199**, 686 (1999).
[16] S. Ceballos, G. Mariotto, S. Murphy, and I. Shvets, Surf. Sci. **523**, 131 (2003).
[17] G. Tarrach, D. Bürgler, T. Schaub, R. Wiesendanger, and H. Güntherodt, Surf. Sci. **285**, 1 (1993).
[18] J. M. Gaines *et al.*, Surf. Sci. **373**, 85 (1997).
[19] Y. J. Kim, Y. Gao, and S. A. Chambers, Surf. Sci. **371**, 358 (1997).
[20] S. A. Chambers, S. Thevuthasan, and S. A. Joyce, Surf. Sci. **450**, L273 (2000).
[21] Y. Gao, Y. Kim, S. Chambers, and G. Bai, J. Vac. Sci. Technol. A **15**, 332 (1997).
[22] J. LaFemina, Crit. Rev. Surf. Chem. **3**, 297 (1994).
[23] G. Mariotto, S. Murphy, and I. V. Shvets, Phys. Rev. B **66**, 245426 (2002).
[24] C. Seoighe, J. Naumann, and I. V. Shvets, Surf. Sci. **440**, 116 (1999).
[25] S. A. Chambers and S. A. Joyce, Surf. Sci. **420**, 111 (1999).
[26] A. Sutton and R. Balluffi, *Interfaces in Crystalline Materials* (Oxford University Press, New York, 1996).
[27] M. Winter, WebElements, http://www.webelements.com
[28] J. A. Meyer, Y. Kuk, P. J. Estrup, and P. J. Silverman, Phys. Rev. B **44**, 9104 (1991).
[29] M. S. Altman and E. Bauer, Surf. Sci. **347**, 265 (1996).